Age-independent seismic anisotropy under oceanic plates explained by strain history in the asthenosphere

Navid Hedjazian [a,*], Fanny Garel [b], D. Rhodri Davies [c], Edouard Kaminski [a]

[a] *Institut de Physique du Globe de Paris, Sorbonne Paris Cité, 75005 Paris, France*
[b] *Géosciences Montpellier, Université de Montpellier, 34095 Montpellier cedex 05, France*
[c] *Research School of Earth Sciences, Australian National University, Canberra, ACT 2601, Australia*

A B S T R A C T

The depth of the oceanic lithosphere–asthenosphere boundary (LAB), as inferred from shear wave velocities, increases with lithospheric age, in agreement with models of cooling oceanic lithosphere. On the other hand, the distribution of radial anisotropy under oceanic plates is almost age-independent. In particular, radial anisotropy shows a maximum positive gradient at a depth of ∼70 km, which, if used as a proxy, indicates an age-independent LAB depth. These contrasting observations have fueled a controversy on the seismological signature of the LAB. To better understand the discrepancy between these observations, we model the development of lattice preferred orientation (LPO) in upper mantle crystal aggregates and predict the seismic anisotropy produced by plate-driven mid-ocean ridge flows. The model accounts for the progressive cooling of the lithosphere with age and can incorporate both diffusion and dislocation creep deformation mechanisms. We find that an age-independent distribution of radial anisotropy is the natural consequence of these simple flows. The depth and strength of anisotropy is further controlled by the deformation regime – dislocation or diffusion creep – experienced by crystals during their ascent towards, and subsequent motion away from, the ridge axis. Comparison to surface wave tomography models yield constraints on rheological parameters such as the activation volume. Although not excluded, additional mechanisms proposed to explain some geophysical signatures of the LAB, such as the presence of partial melt or changes in water content, are not required to explain the radial anisotropy proxy. Our prediction, that the age-independent radial anisotropy proxy marks the transition to flow-induced asthenospheric anisotropy, provides a way to reconcile thermal, mechanical and seismological views of the LAB.

© 2016 Elsevier B.V. All rights reserved.

1. Introduction

The transition from the lithosphere to the asthenosphere is crucial to Earth dynamics, as it couples deep mantle convection to surface plate motion, and marks variations in multiple physical and chemical properties of the Earth such as composition, rheology, electrical conductivity or seismic velocities. We take interest in the lithosphere–asthenosphere boundary (LAB), which is defined as the 'thermo-mechanical' boundary separating the cold and rigid upper lid from the more ductile layer underneath (Fischer et al., 2010). The thermal evolution of oceanic lithosphere and the depth evolution of ocean basins are well-described by the model of a cooling, rigid lithospheric plate, which thickens with age through vertical heat conduction as it moves away from the

ridge axis (Doin and Fleitout, 1996; McKenzie et al., 2005). The transition to the weaker underlying asthenosphere, therefore, is also expected to deepen as a function of plate age, although such a trend is not consistently observed by the seismic data used to map the LAB depth (e.g. vertical changes in seismic wave velocities or seismic anisotropy; Fischer et al., 2010; Rychert et al., 2012; Burgos et al., 2014). As a result, a great deal of uncertainty remains surrounding the depth, nature and pervasiveness of the seismic LAB.

In terms of seismic velocities, the lithosphere is associated with a high velocity region, which contrasts with the low velocity zone (LVZ) associated with the asthenosphere. The decrease in shear wave velocity, which is often used as a proxy for the LAB, is found at a depth that increases with plate age (Burgos et al., 2014; Beghein et al., 2014), which is consistent with the aforementioned model of a cooling oceanic plate. The detection of a sharp drop of wave velocities at the top of the LVZ, called the Gutenberg (G) discontinuity, has also been interpreted as the seismic signature
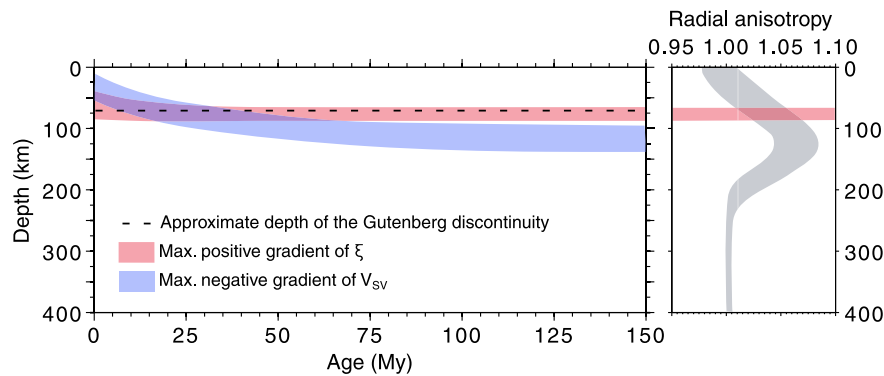

Fig. 1. Summary of seismic observations that are used as a proxy for the LAB. The depth of the Gutenberg discontinuity is estimated from high-frequency techniques (Gaherty et al., 1999; Rychert and Shearer, 2009; Schmerr, 2012). The typical range of profiles of radial anisotropy ξ (in gray) displays a maximum at ∼120 km depth and a maximum positive gradient at ∼70 km depth.

of the LAB (Gutenberg, 1948). The presence of the G discontinuity has been confirmed through high-frequency techniques (Gaherty et al., 1999; Kawakatsu et al., 2009; Rychert and Shearer, 2009; Schmerr, 2012), although its origin, relation to the LAB, and age-dependence remain unclear. This discontinuity is occasionally observed at a shallower depth than the LAB, leading to the hypothesis that yet another, distinct interface is present at this depth (Beghein et al., 2014). The mechanisms underlying this discontinuity are proposed to be changes in seismic anisotropy (Rychert et al., 2012; Beghein et al., 2014), pressure induced compositional variations (Gaherty et al., 1999; Karato, 2012), or partial melt brought to the base of the lithosphere by dynamic processes (Hirschmann, 2010; Schmerr, 2012).

When considering azimuthal seismic anisotropy, the asthenosphere can be defined as a layer with a strong azimuthal anisotropy where the axis of fast propagation is oriented subparallel to the direction of plate motion. The lithosphere is expected to display a frozen-in anisotropy signature, with a fast axis subparallel to the paleo-spreading direction of oceanic plates (Smith et al., 2004; Burgos et al., 2014; Beghein et al., 2014). The change in the offset between the fast axis and the plate motion deepens with plate age, further supporting a thermal origin for the LAB (Beghein et al., 2014; Burgos et al., 2014; Debayle and Ricard, 2013). In the Pacific ocean, another shallower change in azimuthal anisotropy could be associated with the Gutenberg discontinuity (Beghein et al., 2014).

The uncertainties surrounding the nature of the LAB and its age–depth relationship are further compounded by a proxy based upon radial seismic anisotropy. The asthenosphere is expected to display strong radial anisotropy, where horizontally-polarized shear waves travel faster than vertically-polarized shear waves ($V_{SH} > V_{SV}$) (Montagner, 1985; Ekström and Dziewonski, 1998; Panning and Romanowicz, 2006; Nettles and Dziewoński, 2008; Kustowski et al., 2008). This strongly anisotropic layer lies between 80 and 250 km under oceanic plates, and is interpreted as a low viscosity channel (Gung et al., 2003), which is consistent with the classical physical interpretation of the LVZ. However, cross-sections of plate-averaged radial anisotropy exhibit a maximum of the positive vertical gradient at an almost age-independent depth of ∼70 km (Fig. 1) (Nettles and Dziewoński, 2008; Burgos et al., 2014; Beghein et al., 2014). If this proxy corresponds to the LAB, then radial anisotropy predicts that the LAB is horizontal and, accordingly, cannot be interpreted as a purely thermal feature.

To interpret the radial anisotropy observation, and gain insight into its relationship to the LAB, we need to investigate the process at its origin. In the asthenosphere, seismic anisotropy occurs due to the large-scale lattice preferred orientation (LPO) of seismically anisotropic crystals, which are deformed through mantle flow. In the lithosphere, both LPO and shape-preferred orientation of heterogeneities are potential mechanisms for producing seismic

anisotropy (Wang et al., 2013). Apparent anisotropy induced by partial melt at the base of the lithosphere has been proposed as a possible explanation for the deviation of radial anisotropy pattern from the thermal structure (Holtzman and Kendall, 2010; Kennett and Furumura, 2015; Hier-Majumder and Drombosky, 2015). Our framework hypothesizes that seismic anisotropy in the lithosphere corresponds to frozen-in LPO of peridotite aggregates previously deformed in the asthenosphere. The LPO is produced by the progressive (differential) deformation of these crystals in the dislocation creep regime (Nicolas and Christensen, 1987; Karato et al., 2008). Different models of polycrystal deformation have been developed to track the evolution of LPO as a function of the aggregate deformation along mantle flow lines (e.g., Chastel et al., 1993; Tommasi et al., 2000). The model D-Rex of Kaminski et al. (2004), which accounts for the effects of both dynamic recrystallization and intra-crystalline plastic deformation, has been validated through comparison with deformation experiments (e.g., Zhang and Karato, 1995), and is widely used to model LPO across a range of geodynamical settings, including ocean basins (Becker et al., 2008; Gallego et al., 2013).

We combine D-Rex with simple mid-ocean ridge flows to examine the pattern of radial anisotropy expected below oceanic lithosphere, and consider a composite dislocation and diffusion creep rheology. We first present the methods used to compute mantle flow and the associated anisotropy. We then describe the influence of model parameters on the predicted seismic anisotropy, and discuss the implications of our results for the relationship between the LAB and radial anisotropy.

2. Methods

2.1. Ridge flow model

To produce a model of surface-driven mantle flow beneath an oceanic plate, we solve the incompressible Stokes and energy equations relevant to mantle convection using Fluidity, a finite-element, control-volume model based upon unstructured discretizations (Davies et al., 2011; Kramer et al., 2012). Our 2D computational domain (Fig. 2) spans the upper mantle between 0 and 660 km depth, with a ridge axis on the left-hand-side and a subduction zone with a fixed dip angle of 45° to the right. Mesh spacing varies from ∼ 2 km near the left and top boundaries to 10 km on the domain's right-hand side.

Initial conditions comprise a plate with an age increasing from the ridge (0 My at $x = 0$ km) to the 'trench' (75 My at $x = 1500$ km), which follows the half-space cooling model. A constant velocity of 2 cm/y, consistent with the prescribed plate age, is imposed on the upper surface and at the right dipping boundary. The
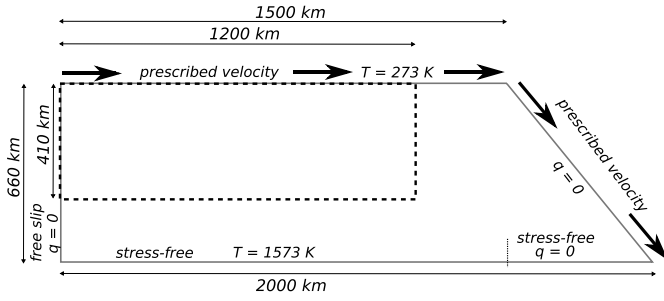
Fig. 2. Simulation domain and boundary conditions for the flow model. At each boundary, either a temperature T or a heat flux q is imposed. Black arrows show the prescribed velocity of 2 cm/y on the upper and right boundaries. We calculate seismic anisotropy in the zone delimited by the dashed box.

bottom surface is stress-free. Zero normal flow is prescribed, by symmetry, on the left boundary. A fixed cold temperature boundary condition (273 K) is prescribed at the surface, and a constant hot temperature (1573 K) is prescribed on the leftmost bottom boundary (between 0 and 1500 km). The remainder of the bottom boundary and the left and right sides of the domain have a zero heat flux boundary condition.

We consider a mantle undergoing deformation through either (i) pure dislocation creep; or (ii) a composite diffusion and dislocation creep (i.e. mixed) rheology. Viscosity is calculated at each time step from the general power law (e.g., Karato and Wu, 1993; Hirth and Kohlstedt, 2003):

$$\mu = A^{-\frac{1}{n}} \exp\left(\frac{E + PV}{nR(T + \delta T)}\right) \dot{\epsilon}_{II}^{\frac{1-n}{n}},$$

where $\dot{\epsilon}_{II}$ is the second invariant of the strain-rate tensor, n is the stress exponent that depends on the deformation mechanism, E and V are activation energy and volume, A is a prefactor, $P = \rho g z$ is the lithostatic pressure (z is depth), R is the gas constant and T is the temperature corrected with an adiabatic gradient $\delta T/\delta z$. Note that the rheological parameters, detailed in Table 1, are chosen to yield realistic upper-mantle viscosity values that are consistent with geophysical constraints, following the methodology of Garel et al. (2014). For the mixed-rheology case, the effective viscosity is calculated via harmonic mean as $(\mu_{\text{diff}}^{-1} + \mu_{\text{disl}}^{-1})^{-1}$ with μ_{diff} and μ_{disl} the viscosity associated to diffusion or dislocation creep, respectively. Note that viscosity is isotropic and does not depend on the strength of the LPO. Once the flow reaches a steady-state, we extract a box of 400 km depth and 1200 km length, within which we compute seismic anisotropy. We restrict the calculation to young ages, where the half-space cooling model and plate model are consistent.

2.2. Calculation of seismic anisotropy

To model LPO evolution by plastic deformation and dynamic recrystallization in the dislocation creep regime, we used the model D-Rex (Kaminski et al., 2004). We consider aggregates of $N \approx 2000$ crystals with 70% olivine and 30% enstatite, which is a first order approximation of a pyrolite model (Nicolas and Christensen, 1987). The aggregates deform progressively along their path line, starting at 400 km depth with an initial random LPO. We assume that olivine crystals which deform by dislocation creep do so on three independent slip systems, among (010)[100], (001)[100], (010)[001] and (100)[001], where () denotes the Miller indices of the slip-plane normal and [] the slip direction. The respective normalized reference resolved shear stresses are $\tau_0^{(010)[100]}$, $\tau_0^{(001)[100]}/\tau_0^{(010)[100]}$, $\tau_0^{(010)[001]}/\tau_0^{(010)[100]}$ and $\tau_0^{(100)[001]}/\tau_0^{(010)[100]}$; their value is given in Table 2 for two types of fabric expected in a dry (A) and wet (E) mantle. Unless

Table 1
Physical parameters used in the simulations, consistent with experimental data (Hirth and Kohlstedt, 2003; Korenaga and Karato, 2008).

Quantity	Symbol	Units	Value
Gravity	g	m s^{-2}	9.8
Thermal expansivity coefficient	α	K^{-1}	3×10^{-5}
Thermal diffusivity	κ	$\text{m}^2\,\text{s}^{-1}$	10^{-6}
Reference density	ρ_s	kg m^{-3}	3300
Cold, surface temperature	T_s	K	273
Hot, mantle temperature	T_m	K	1573
Adiabatic temperature gradient	$\delta T/\delta z$	K km^{-1}	0.5
Gas constant	R	$\text{J K}^{-1}\,\text{mol}^{-1}$	8.3145
Max. viscosity	μ_{max}	Pa s	10^{25}
Min. viscosity	μ_{min}	Pa s	10^{18}
Diffusion creep			
Activation energy	E	kJ mol^{-1}	300
Activation volume	V	$\text{cm}^3\,\text{mol}^{-1}$	4
Prefactor	A	$\text{Pa}^{-1}\,\text{s}^{-1}$	3.0×10^{-11}
	n	–	1
Dislocation creep (UM)			
Activation energy	E	kJ mol^{-1}	540
Activation volume	V	$\text{cm}^3\,\text{mol}^{-1}$	12
Prefactor	A	$\text{Pa}^{-n}\,\text{s}^{-1}$	5.0×10^{-16}
	n	–	3.5

Table 2
Resolved shear stress of the different olivine slip systems for each fabric type, after (Kaminski et al., 2004) and (Becker et al., 2008).

Fabric type	(010)[100]	(100)[100]	(010)[001]	(100)[001]
A	1	2	3	∞
E	2	1	∞	3

otherwise indicated, other parameters are taken as in the reference D-Rex model (Kaminski and Ribe, 2001; Kaminski et al., 2004).

LPO evolution under diffusion creep is still debated. Deformation in the diffusion creep regime is not expected to produce a coherent rotation of the crystallographic axes in a crystal aggregate, hence is not expected to produce LPO (Karato and Wu, 1993). But insights from numerical modeling (Wheeler, 2009) and olivine deformation experiments (Miyazaki et al., 2013) in the diffusion creep regime indicate that the crystals may preserve their LPO. Diffusion creep effect on LPO is usually taken into account by scaling the strain-rate tensor by the percentage of strain accommodated by dislocation creep (Becker et al., 2008). Under this assumption, the crystals are rotated as a rigid body within the fluid in the pure diffusion creep regime (0% of strain accommodated by dislocation creep). However the aggregate effectively accommodates the strain (by diffusion creep and grain boundary sliding) with a change of shape, thus modifying the lattice orientation. To take this into account, we assume that the crystals are not rotated by the rigid body rotation but rather by the deformation fluid rotation, i.e. the rotation of the finite strain ellipsoid (McKenzie and Jackson, 1983). Since all crystals endure the same rotation, this model can neither reinforce nor weaken the strength of the LPO. We calculate the bulk rotation of the LPO by multiplying the matrix of direction cosines of the aggregates with the rotation of the finite strain ellipsoid given analytically by Ribe (1992). We do not consider any randomization of the relative orientations of the crystals, that could be produced by grain boundary sliding. The effect on the re-orientation of the mean olivine lattice orientation in the diffusion creep regime is shown in Supplementary Material, Fig. S1.

From a given LPO, the elastic tensor is calculated by a Voigt average. We do not include effects of grain size, temperature or pressure on the elastic tensor of the aggregates, as they do not significantly affect the anisotropic properties (e.g., da Silva et al., 1997). Love and azimuthal parameters are calculated directly from the Voigt averaged tensor (Montagner and Nataf, 1986):
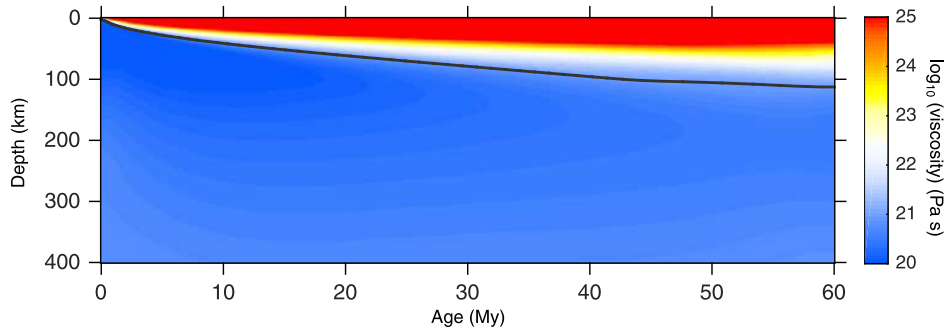
Fig. 3. Viscosity (log scale) produced by a mid-ocean ridge flow model with a mixed rheology and $V_{disl} = 12$ cm^3/mol. The black contour marks $\mu = 10^{21}$ Pa s. (For interpretation of the colors in this figure, the reader is referred to the web version of this article.)

$$L = \frac{1}{2}(C_{44} + C_{55}),$$

$$N = \frac{1}{8}(C_{11} + C_{22}) - \frac{1}{4}C_{12} + \frac{1}{2}C_{66},$$

$$G_c = \frac{1}{2}(C_{55} - C_{44}),$$

$$G_s = C_{54}.$$

In order to mimic surface-wave inversion, we represent the radial anisotropy parameter as $\xi = N/L$, and the strength or % of azimuthal anisotropy as $G = \sqrt{G_c^2 + G_s^2}$.

3. Results

The rheology of upper mantle crystal aggregates (mainly olivine) is constrained through laboratory experiments, from which maps of deformation mechanism can be established as a function of key parameters such as temperature, pressure, stress and grain size (e.g., Hirth and Kohlstedt, 2003). Extrapolation of laboratory flow laws to mantle conditions suggests that upper mantle deformation lies close to the boundary between diffusion and dislocation creep regimes. Our flow model maps out the upper mantle regions likely to be deforming preferentially through dislocation or diffusion creep, as a function of temperature, pressure and strain rate. As already mentioned, intra-crystalline plastic deformation by dislocation creep is key to producing LPO and, hence, seismic anisotropy, whereas diffusion creep and related mechanisms such as grain boundary sliding do not produce a coherent rotation of the crystallographic axes in a crystal aggregate and, hence, do not produce LPO. As such, variations of seismic anisotropy could be a consequence of a local change in deformation mechanism.

To test this hypothesis, we compare the mantle flow model undergoing deformation through pure dislocation creep with the mixed-rheology model. Our flow models naturally develop an age-dependent thermo-mechanical boundary layer at the top of the domain, that accounts for the rigid lithosphere (Fig. 3). We find that the different rheologies between the two models have little impact on the resulting flow field and the spatial distribution of strain rate and temperature (Fig. 4), in agreement with analytical flows (Hedjazian and Kaminski, 2014). Within the parameter space investigated herein, rheology will thus only affect LPO development through the relative spatial extent of the zones where deformation occurs by dislocation creep (Fig. 4c), and we next quantify these differences.

LPO development in the dislocation creep regime depends on intra-crystalline plastic deformation, which, itself, is a function of the relative strength of the slip systems. Here we use the reference resolved shear stresses determined for dry olivine, which corresponds to an A-type fabric and where the fast axis of crystals

tends to align with the flow direction (Karato et al., 2008). The second mechanism driving LPO development in the mantle is dynamic recrystallization. In D-Rex, the key parameter controlling the rate of LPO evolution through dynamic recrystallization is the (dimensionless) grain boundary mobility, M^* (Kaminski et al., 2004). A value of $M^* = 125 \pm 50$ is required to reproduce the LPO obtained in laboratory experiments for uniform deformation and a random initial LPO (Kaminski et al., 2004). This value is used for simulating the development of LPO through D-Rex on a regular basis. A recent study, however, has shown that in the case of a non-random initial LPO, a value of $M^* = 10$ is required to fit the experimental results (Boneh et al., 2015). This low value of M^* is likely more appropriate for modeling seismic anisotropy near mid-ocean ridges, where the shear direction varies along flow lines in the convecting mantle. We thus consider below the impact of M^* on the model outputs.

As a first step in simulating mid-ocean ridge LPO development and the associated seismic anisotropy, we use the classical value of $M^* = 125$, and consider a pure dislocation creep regime (a pure diffusion creep regime would not produce any LPO). We then compare the predicted seismic anisotropy to the results of global surface wave tomography, which provide insight into large-scale anisotropy patterns. Our model predicts a layer with a strong radial anisotropy ($\xi \sim 1.1$), from $\sim$20–100 km depth, at 60 My, with radial anisotropy disappearing at greater depths due to the oblique orientation of the aggregate fast axis (Fig. 5). Furthermore, the strength of azimuthal anisotropy can reach up to 6% (Supplementary Material, Fig. S2). Such high values of anisotropy are not observed at a large scale in the upper mantle (Panning and Romanowicz, 2006; Nettles and Dziewoński, 2008; Burgos et al., 2014; Beghein et al., 2014), implying that this combination of parameters overestimates the strength of LPO.

We next examine a case with $M^* = 10$, which leads to slower LPO evolution and, hence, a decrease in the strength of seismic anisotropy. This lower value of M^* produces a radial anisotropy smaller than 1.1 (Fig. 6a) and 2–4% of azimuthal anisotropy (Supplementary Material, Fig. S3), which correspond to the estimates of anisotropy in the asthenosphere. The strength of anisotropy predicted by the model in the lithosphere ($\xi > 1.05$), and at depths greater than 250 km, however, exceeds observations (Smith et al., 2004; Panning and Romanowicz, 2006; Nettles and Dziewoński, 2008; Kustowski et al., 2008; Debayle and Ricard, 2013; Beghein et al., 2014).

In the mixed-rheology flow model (keeping $M^* = 10$ in the zones where deformation occurs by dislocation creep), lithospheric anisotropy and anisotropy at >250 km depth is weaker and more consistent with observations (Fig. 6b). The variations of seismic anisotropy in the upper mantle reflect the change in deformation history of crystals along flow lines, as they ascend towards and subsequently move away from the ridge axis (Fig. 4). The deformation experienced by crystals along ascending flow lines close
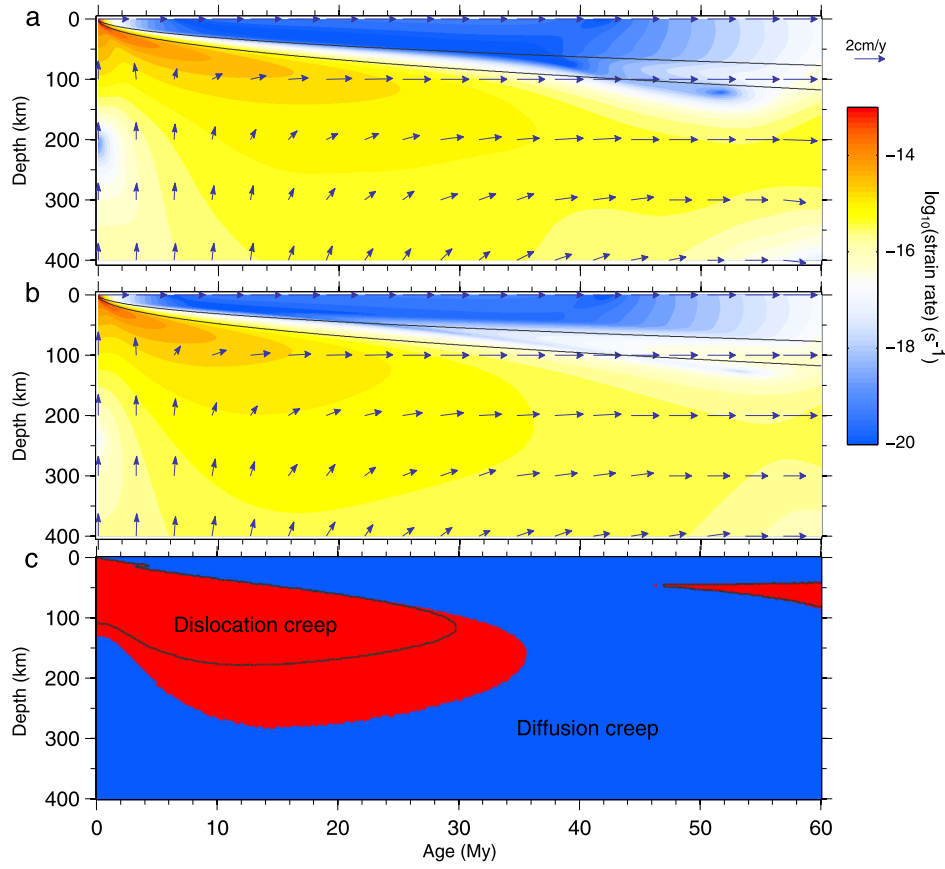
Fig. 4. Mid-ocean ridge flow models. The strain-rate second invariant $\dot{\varepsilon}$ (colormap) and flow velocity (blue arrows) fields are practically indistinguishable between a model deforming solely through dislocation creep (**a**) and a model with a composite diffusion and dislocation creep rheology (**b**). Solid gray lines delineate the 1300 K and 1500 K isotherms. (**c**) Displays the dominant deformation mechanism, dislocation creep (red) or diffusion creep (blue) in the model with mixed rheology and $V_{disl} = 12$ cm^3/mol. The black line shows the boundary between the two mechanisms for a model with mixed rheology and $V_{disl} = 16$ cm^3/mol. (For interpretation of the colors in this figure, the reader is referred to the web version of this article.)
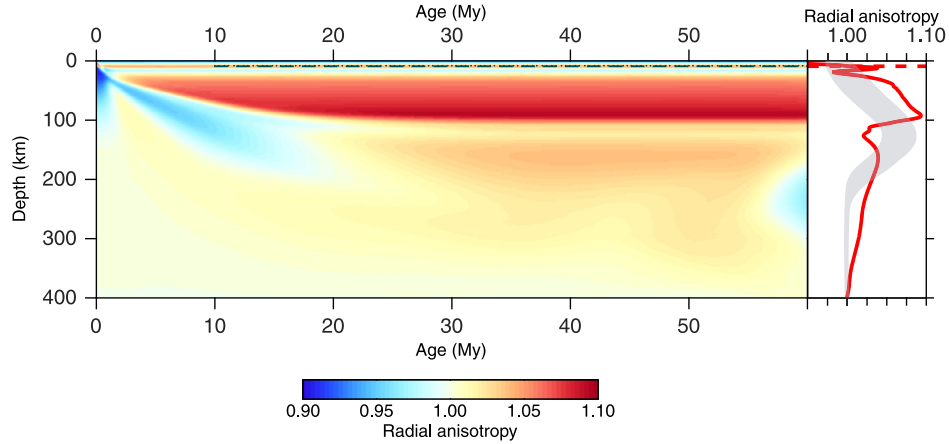

Fig. 5. Radial anisotropy prediction of the model for the D-Rex reference parameter values, i.e. a pure dislocation creep rheology and $M^* = 125$. Dashed lines show the depth of the maximum positive gradient of radial anisotropy. The right panel shows the radial anisotropy profile at 40 My. The gray zone is the range of profiles seen at moderate age in ocean basins in the literature (as in Fig. 1). (For interpretation of the colors in this figure, the reader is referred to the web version of this article.)

to the ridge axis occurs mainly in the diffusion creep regime, and corresponds to a vertical shear direction. It creates a moderate LPO, with the average fast axis of the crystal aggregates remaining oblique to the horizontal flow direction and, accordingly, does not produce a strong radial anisotropy. On the other hand, crystals deformed along flow lines in the asthenosphere, away from the ridge axis (5–30 My) experience mainly dislocation creep and horizontal shear. They develop a strong LPO with a sub-horizontal fast axis, which results in a strong radial

anisotropy. Last, crystal aggregates located below 250 km depth deform solely through diffusion creep and do not produce any LPO, which is consistent with tomographic models where seismic anisotropy vanishes below ~250 km depth (Montagner, 1985; Ekström and Dziewonski, 1998; Nettles and Dziewoński, 2008; Burgos et al., 2014).

As variations in water content have been proposed to play a key role in the LAB and G discontinuity (e.g., Gaherty et al., 1999; Karato et al., 2008; Karato, 2012; Beghein et al., 2014), we consider,
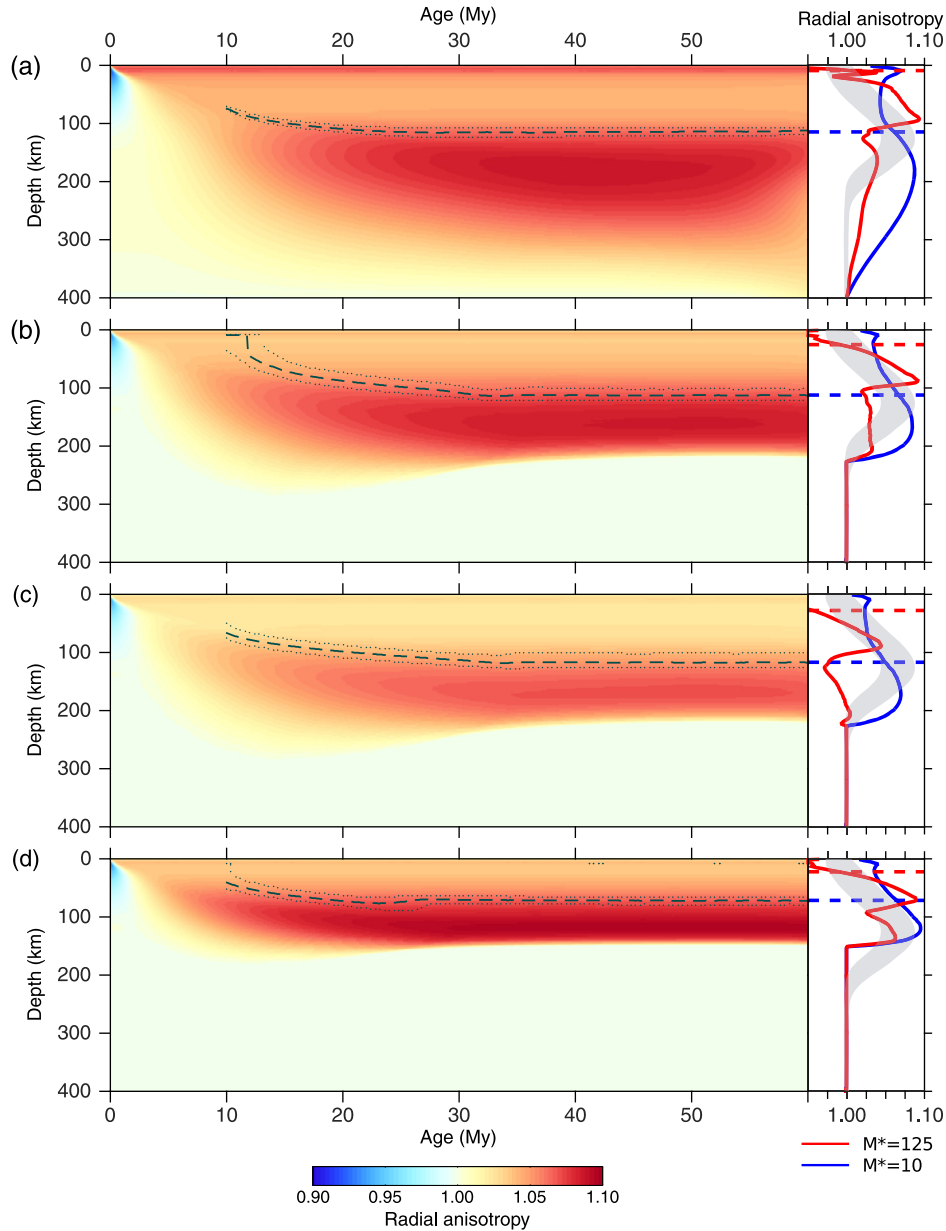
Fig. 6. **Radial anisotropy** ξ **with slow dynamic recrystallization** ($M^* = 10$)**, and for different rheologies and parameters used in the calculation of LPO development.** (**a**) Pure dislocation creep; (**b**) mixed rheology, A-type olivine fabric; (**c**) mixed rheology, E-type olivine fabric; (**d**) mixed rheology, A-type olivine fabric and $V_{disl} = 16$ cm^3/mol; As in Fig. 5, dashed lines show the depth of the maximum positive gradient of radial anisotropy, with 5% range of the gradient value around the maximum (dotted lines) demonstrating the robustness of the prediction. The radial anisotropy profile tends to stabilize starting from 30 My. The profiles at 40 My highlight the effect of the rate of LPO evolution, between $M^* = 10$ (blue line) and $M^* = 125$ (red line). Dashed blue and red lines mark the corresponding maximum positive gradient of radial anisotropy. (For interpretation of the colors in this figure, the reader is referred to the web version of this article.)

as a final case, the impact of water on the anisotropy predicted in our model. Following the conclusion of the previous part of the section, we consider slow dynamic recrystallization ($M^* = 10$) and a mixed rheology. In the presence of water, olivine deformation leads to an E-type fabric, which produces a moderate radial anisotropy and a stronger azimuthal anisotropy compared to A-type fabric. E-type induced anisotropy, however, follows a similar pattern to the A-type fabric (Fig. 6c). These fabric types and, hence, water content of Earth's upper mantle, can be discriminated only by the amplitude of seismic anisotropy, which cannot be robustly constrained by global tomography models. Dehydration of olivine as material upwells under the ridge could trigger an E- to A-type fabric transition, and would lead to an increase of radial anisotropy at shallower depths. As this is not observed in the surface wave tomography models, two possible interpretations remain. Either:

(i) changes in olivine hydration are not in the adequate range to cause a fabric transition; or (ii) its effects on seismic anisotropy are not captured at the current resolution of tomography models. In summary, these radial anisotropy observations do not constrain the amount of water in the upper mantle.

4. Discussion

To discuss the implications of our results for the interpretation of the LAB defined using the radial anisotropy proxy, we compute the depth of the maximum positive gradient of radial anisotropy for all cases examined (Fig. 6). For fast LPO development ($M^* = 125$), the maximum gradient is produced as material upwells under the ridge axis and is subsequently frozen into the lithosphere. This occurs at too shallow a depth (<25 km)

to be considered as a consistent proxy for the LAB (Fig. 5). For slower LPO development ($M^* = 10$), the depth of the maximum gradient lies at ∼100 km and becomes independent of plate age in relatively young lithosphere (∼20–30 My), which is more compatible with surface-wave observations (Burgos et al., 2014; Beghein et al., 2014). At older ages, the combination of a shear direction that is close to the horizontal plane and strain rates that are several orders of magnitude less than those experienced close to the ridge axis reduce the probability of overprinting existing fabric on a large scale, which leads to the apparent 'frozen' signature of radial anisotropy.

We explored the parameter space for both diffusion and dislocation creep deformation laws by systematically varying the values of activation energy, activation volume, rheological prefactor and stress exponent in our mantle flow models. Our results demonstrate that the horizontal layering of radial anisotropy is a robust signature of LPO evolution in a mid-ocean ridge setting (Fig. 6, Supplementary Material Fig. S4 to S8). The spatial distribution of dislocation and diffusion creep controls the strength of anisotropy, ranging from isotropic for pure diffusion creep to strongly anisotropic for pure dislocation creep (Fig. 6a). The depth range of the strong radially anisotropic layer depends on the depth at which dislocation creep dominates over diffusion creep. This is principally controlled by the activation volumes of dislocation creep, V_{disl}, and diffusion creep, V_{diff} (Fig. 6d, Supplementary Material Fig. S4). These parameters are not tightly constrained by experimental measurements (Korenaga and Karato, 2008). A typical value of $V_{\text{disl}} = 12$ cm^3/mol yields a maximum positive gradient of radial anisotropy at ∼100 km depth (Fig. 6b). With a value of $V_{\text{disl}} = 16$ cm^3/mol, the maximum positive gradient lies at a depth of ∼70 km (Fig. 6d), in better agreement with observations from surface wave tomography (Burgos et al., 2014). Such a high value of V_{disl} has been experimentally measured and also correctly predicts the depth of the LVZ (Raterron et al., 2011).

We now discuss the reliability of the parameter values chosen in our preferred model. The disappearance of radial anisotropy at depths of >250 km has long been used to support the dominance of diffusion creep in the deep upper mantle (Karato and Wu, 1993). The typical values chosen in this study allow to reproduce this observation. However, this is also possible for a range of values for the parameters in the viscosity laws (E, V and A for each deformation mechanism). The (relatively) strong depth resolution of surface waves suggests that the existence of a layer of strong radial anisotropy at the base of the lithosphere is robust. Our inferred values of M^* and V_{disl} rely on this observation and are confirmed by constrains from complementary methods (Boneh et al., 2015; Raterron et al., 2011). Other parameters, such as the % of olivine in the composition, the E- or A-type fabric, are chosen to match the amplitude of seismic anisotropy parameters, which are affected by the regularization of the corresponding global tomography models. Their value is thus bonded to this uncertainty.

Relating our predictions to the G discontinuity is appealing but not straightforward. It has been identified as a sharp (≤20 km) discontinuity in the Pacific basin, and is influenced by regional processes (e.g., Schmerr, 2012). Radial anisotropy, on the contrary, is mostly observed by surface wave tomography, which samples large regions of the upper mantle and is an averaged quantity. It is therefore well explained by our interpretation of radial anisotropy originating from a global, age-independent structure near the LAB. Observations of radial anisotropy, in more detailed, higher-resolution studies, may reveal a greater complexity in the radial anisotropy pattern. Our 2D framework does not account for such observations, and refinement would require regional flow modeling, and taking into account sources of seismic anisotropy other than LPO. On top of the LPO-induced anisotropy, local occurrences of partial melt at the base of the lithosphere could produce radial anisotropy with similar characteristics, with a maximum gradient of ξ between 60 and 100 km depth (Kennett and Furumura, 2015). Predicting the effect of variations in olivine hydration on LPO requires an accurate knowledge of water content, as it could trigger fabric transitions (Karato et al., 2008), but we showed that the different fabrics are difficult to distinguish using seismological observations. These arguments suggest that water or partial melt may not significantly distrust the plate-driven radial anisotropy profile predicted here. However these mechanisms also impact on the rheological laws and, accordingly, the strain rate and resulting seismic anisotropy. Additionally, the effect of small amounts of partial melt on the development of olivine LPO is largely unknown. This complex interplay makes it difficult confidently relate variations in radial anisotropy to the G discontinuity. On the contrary, the G discontinuity could be related to changes in azimuthal anisotropy, which has been observed by various methods with complementary sensitivities (Rychert et al., 2012; Beghein et al., 2014). Our model shows that a simple plate-driven 2D flow does not produce azimuthal anisotropy variations explaining the G discontinuity (Supplementary Material, Fig. S3). Fully account for 3D and density-driven mantle flow (e.g., Becker et al., 2014) will be required to further constrain our model using variations of azimuthal anisotropy.

5. Conclusion

We have demonstrated that LPO evolution in a 2D plate-driven flow yields an age-independent profile of radial anisotropy, which is compatible with tomographic observations. Ad hoc mechanisms at the LAB proposed in the literature to explain age-independent discontinuities, such a dehydration or partial melt, do not appear necessary in the case of the radial anisotropy proxy. With a composite diffusion and dislocation creep rheology and a slow dynamic recrystallization, the maximum positive gradient of radial anisotropy is predicted at a depth depending mainly on the activation volumes of the olivine creep laws. Such a prediction provides an interpretation for the distribution of radial anisotropy near the LAB, thus reconciling the seismic observables with thermo-mechanical models of the lithosphere: if the age-dependent LAB, identified from shear-wave velocity and azimuthal anisotropy proxies, is of thermal origin, the age-independent radial anisotropy proxy reflects the natural strain history of crystals under a simple surface-driven mid-ocean ridge flow regime. The Gutenberg discontinuity, and possible associated variations in azimuthal anisotropy, remain to be explained.

Appendix A. Supplementary material

Supplementary material related to this article can be found online at http://dx.doi.org/10.1016/j.epsl.2016.12.004.

References

Becker, T.W., Conrad, C.P., Schaeffer, A.J., Lebedev, S., 2014. Origin of azimuthal seismic anisotropy in oceanic plates and mantle. Earth Planet. Sci. Lett. 401, 236–250. http://dx.doi.org/10.1016/j.epsl.2014.06.014.

Becker, T.W., Kustowski, B., Ekström, G., 2008. Radial seismic anisotropy as a constraint for upper mantle rheology. Earth Planet. Sci. Lett. 267 (1), 213–227. http://dx.doi.org/10.1016/j.epsl.2007.11.038.

Beghein, C., Yuan, K., Schmerr, N., Xing, Z., 2014. Changes in seismic anisotropy shed light on the nature of the Gutenberg discontinuity. Science 343 (6176), 1237–1240. http://dx.doi.org/10.1126/science.1246724.

Boneh, Y., Morales, L.F., Kaminski, E., Skemer, P., 2015. Modeling olivine CPO evolution with complex deformation histories-implications for the interpretation of seismic anisotropy in the mantle. Geochem. Geophys. Geosyst. 16 (10), 3436–3455. http://dx.doi.org/10.1002/2015GC005964.

Burgos, G., Montagner, J.-P., Beucler, E., Capdeville, Y., Mocquet, A., Drilleau, M., 2014. Oceanic lithosphere–asthenosphere boundary from surface wave dispersion data. J. Geophys. Res., Solid Earth 119 (2), 1079–1093. http://dx.doi.org/10.1002/2013JB010528.

Chastel, Y.B., Dawson, P.R., Wenk, H.-R., Bennett, K., 1993. Anisotropic convection with implications for the upper mantle. J. Geophys. Res. 98 (B10), 17757–17771. http://dx.doi.org/10.1029/93JB01161.

da Silva, C., Stixrude, L., Wentzcovitch, R.M., 1997. Elastic constants and anisotropy of forsterite at high pressure. Geophys. Res. Lett. 24 (15), 1963–1966. http://dx.doi.org/10.1029/97GL01756.

Davies, D.R., Wilson, C.R., Kramer, S.C., 2011. Fluidity: a fully unstructured anisotropic adaptive mesh computational modeling framework for geodynamics. Geochem. Geophys. Geosyst. 12 (6). http://dx.doi.org/10.1029/2011GC003551.

Debayle, E., Ricard, Y., 2013. Seismic observations of large-scale deformation at the bottom of fast-moving plates. Earth Planet. Sci. Lett. 376, 165–177. http://dx.doi.org/10.1016/j.epsl.2013.06.025.

Doin, M., Fleitout, L., 1996. Thermal evolution of the oceanic lithosphere: an alternative view. Earth Planet. Sci. Lett. 142 (1), 121–136. http://dx.doi.org/10.1016/0012-821X(96)00082-9.

Ekström, G., Dziewonski, A.M., 1998. The unique anisotropy of the pacific upper mantle. Nature 394 (6689), 168–172. http://dx.doi.org/10.1038/28148.

Fischer, K.M., Ford, H.A., Abt, D.L., Rychert, C.A., 2010. The lithosphere–asthenosphere boundary. Annu. Rev. Earth Planet. Sci. 38, 551–575. http://dx.doi.org/10.1146/annurev-earth-040809-152438.

Gaherty, J.B., Kato, M., Jordan, T.H., 1999. Seismological structure of the upper mantle: a regional comparison of seismic layering. Phys. Earth Planet. Inter. 110 (1), 21–41. http://dx.doi.org/10.1016/S0031-9201(98)00132-0.

Gallego, A., Ito, G., Dunn, R., 2013. Investigating seismic anisotropy beneath the Reykjanes Ridge using models of mantle flow, crystallographic evolution, and surface wave propagation. Geochem. Geophys. Geosyst. 14 (8), 3250–3267. http://dx.doi.org/10.1002/ggge.20204.

Garel, F., Goes, S., Davies, D., Davies, J., Kramer, S., Wilson, C., 2014. Interaction of subducted slabs with the mantle transition-zone: a regime diagram from 2-d thermo-mechanical models with a mobile trench and an overriding plate. Geochem. Geophys. Geosyst. 15 (5), 1739–1765. http://dx.doi.org/10.1002/2014GC005257.

Gung, Y., Panning, M., Romanowicz, B., 2003. Global anisotropy and the thickness of continents. Nature 422 (6933), 707–711. http://dx.doi.org/10.1038/nature01559.

Gutenberg, B., 1948. On the layer of relatively low wave velocity at a depth of about 80 kilometers. Bull. Seismol. Soc. Am. 38 (2), 121–148.

Hedjazian, N., Kaminski, E., 2014. Defining a proxy for the interpretation of seismic anisotropy in non-newtonian mantle flows. Geophys. Res. Lett. 41 (20), 7065–7072. http://dx.doi.org/10.1002/2014GL061372.

Hier-Majumder, S., Drombosky, T., 2015. Development of anisotropic contiguity in deforming partially molten aggregates: 2. Implications for the lithosphere–asthenosphere boundary. J. Geophys. Res., Solid Earth 120 (2), 764–777. http://dx.doi.org/10.1002/2014JB011454.

Hirschmann, M.M., 2010. Partial melt in the oceanic low velocity zone. Phys. Earth Planet. Inter. 179 (1), 60–71. http://dx.doi.org/10.1016/j.pepi.2009.12.003.

Hirth, G., Kohlstedt, D., 2003. Rheology of the upper mantle and the mantle wedge: a view from the experimentalists. In: Inside the Subduction Factory. Wiley-Blackwell, pp. 83–105.

Holtzman, B., Kendall, J.-M., 2010. Organized melt, seismic anisotropy, and plate boundary lubrication. Geochem. Geophys. Geosyst. 11 (12). http://dx.doi.org/10.1029/2010GC003296.

Kaminski, E., Ribe, N., 2001. A kinematic model for recrystallization and texture development in olivine polycrystals. Earth Planet. Sci. Lett. 189 (3), 253–267. http://dx.doi.org/10.1016/S0012-821X(01)00356-9.

Kaminski, E., Ribe, N.M., Browaeys, J.T., 2004. D-Rex, a program for calculation of seismic anisotropy due to crystal lattice preferred orientation in the convective upper mantle. Geophys. J. Int. 158 (2), 744–752. http://dx.doi.org/10.1111/j.1365-246X.2004.02308.x.

Karato, S.-I., 2012. On the origin of the asthenosphere. Earth Planet. Sci. Lett. 321, 95–103. http://dx.doi.org/10.1016/j.epsl.2012.01.001.

Karato, S.-I., Jung, H., Katayama, I., Skemer, P., 2008. Geodynamic significance of seismic anisotropy of the upper mantle: new insights from laboratory studies. Annu. Rev. Earth Planet. Sci. 36, 59–95. http://dx.doi.org/10.1146/annurev.earth.36.031207.124120.

Karato, S.-I., Wu, P., 1993. Rheology of the upper mantle: a synthesis. Science 260 (5109), 771–778. http://dx.doi.org/10.1126/science.260.5109.771.

Kawakatsu, H., Kumar, P., Takei, Y., Shinohara, M., Kanazawa, T., Araki, E., Suyehiro, K., 2009. Seismic evidence for sharp lithosphere–asthenosphere boundaries of oceanic plates. Science 324 (5926), 499–502. http://dx.doi.org/10.1126/science.1169499.

Kennett, B., Furumura, T., 2015. Toward the reconciliation of seismological and petrological perspectives on oceanic lithosphere heterogeneity. Geochem. Geophys. Geosyst. http://dx.doi.org/10.1002/2015GC006017.

Korenaga, J., Karato, S.-I., 2008. A new analysis of experimental data on olivine rheology. J. Geophys. Res., Solid Earth 113 (B2). http://dx.doi.org/10.1029/2007JB005100.

Kramer, S.C., Wilson, C.R., Davies, D.R., 2012. An implicit free surface algorithm for geodynamical simulations. Phys. Earth Planet. Inter. 194, 25–37. http://dx.doi.org/10.1016/j.pepi.2012.01.001.

Kustowski, B., Ekström, G., Dziewoński, A., 2008. Anisotropic shear-wave velocity structure of the Earth's mantle: a global model. J. Geophys. Res. 113 (B06306). http://dx.doi.org/10.1029/2007JB005169.

McKenzie, D., Jackson, J., 1983. The relationship between strain rates, crustal thickening, paleomagnetism, finite strain and fault movements within a deforming zone. Earth Planet. Sci. Lett. 65 (1), 182–202.

McKenzie, D., Jackson, J., Priestley, K., 2005. Thermal structure of oceanic and continental lithosphere. Earth Planet. Sci. Lett. 233 (3), 337–349. http://dx.doi.org/10.1016/j.epsl.2005.02.005.

Miyazaki, T., Sueyoshi, K., Hiraga, T., 2013. Olivine crystals align during diffusion creep of Earth's upper mantle. Nature 502 (7471), 321–326. http://dx.doi.org/10.1038/nature12570.

Montagner, J.-P., 1985. Seismic anisotropy of the Pacific Ocean inferred from long-period surface waves dispersion. Phys. Earth Planet. Inter. 38 (1), 28–50. http://dx.doi.org/10.1016/0031-9201(85)90120-7.

Montagner, J.-P., Nataf, H.-C., 1986. A simple method for inverting the azimuthal anisotropy of surface waves. J. Geophys. Res. 91 (B1), 511–520. http://dx.doi.org/10.1029/JB091iB01p00511.

Nettles, M., Dziewoński, A.M., 2008. Radially anisotropic shear velocity structure of the upper mantle globally and beneath North America. J. Geophys. Res. 113 (B02303). http://dx.doi.org/10.1029/2006JB004819.

Nicolas, A., Christensen, N.I., 1987. Formation of anisotropy in upper mantle peridotites: a review. In: Fuchs, K., Froidevaux, C. (Eds.), Composition, Structure and Dynamics of the Lithosphere–Asthenosphere System. AGU, Washington, D.C., pp. 111–123.

Panning, M., Romanowicz, B., 2006. A three-dimensional radially anisotropic model of shear velocity in the whole mantle. Geophys. J. Int. 167 (1), 361–379. http://dx.doi.org/10.1111/j.1365-246X.2006.03100.x.

Raterron, P., Chen, J., Geenen, T., Girard, J., 2011. Pressure effect on forsterite dislocation slip systems: implications for upper-mantle LPO and low viscosity zone. Phys. Earth Planet. Inter. 188 (1), 26–36. http://dx.doi.org/10.1016/j.pepi.2011.06.009.

Ribe, N.M., 1992. On the relation between seismic anisotropy and finite strain. J. Geophys. Res. 97 (B6), 8737–8747. http://dx.doi.org/10.1029/92JB00551.

Rychert, C.A., Schmerr, N., Harmon, N., 2012. The pacific lithosphere–asthenosphere boundary: seismic imaging and anisotropic constraints from ss waveforms. Geochem. Geophys. Geosyst. 13 (9). http://dx.doi.org/10.1029/2012GC004194.

Rychert, C.A., Shearer, P.M., 2009. A global view of the lithosphere–asthenosphere boundary. Science 324 (5926), 495–498. http://dx.doi.org/10.1126/science.1169754.

Schmerr, N., 2012. The Gutenberg discontinuity: melt at the lithosphere–asthenosphere boundary. Science 335 (6075), 1480–1483. http://dx.doi.org/10.1126/science.1215433.

Smith, D.B., Ritzwoller, M.H., Shapiro, N.M., 2004. Stratification of anisotropy in the pacific upper mantle. J. Geophys. Res. 109 (B11). http://dx.doi.org/10.1029/2004JB003200.

Tommasi, A., Mainprice, D., Canova, G., Chastel, Y., 2000. Viscoplastic self-consistent and equilibrium-based modeling of olivine lattice preferred orientations: implications for the upper mantle seismic anisotropy. J. Geophys. Res. 105 (B4), 7893–7908. http://dx.doi.org/10.1029/1999JB900411.

Wang, N., Montagner, J.-P., Fichtner, A., Capdeville, Y., 2013. Intrinsic versus extrinsic seismic anisotropy: the radial anisotropy in reference earth models. Geophys. Res. Lett. 40 (16), 4284–4288. http://dx.doi.org/10.1002/grl.50873.

Wheeler, J., 2009. The preservation of seismic anisotropy in the Earth's mantle during diffusion creep. Geophys. J. Int. 178 (3), 1723–1732. http://dx.doi.org/10.1111/j.1365-246X.2009.04241.x.

Zhang, S., Karato, S.-I., 1995. Lattice preferred orientation of olivine aggregates deformed in simple shear. Nature 375 (6534), 774–777. http://dx.doi.org/10.1038/375774a0.